

Stress in three-dimensionally integrated sensor systems



Lado Filipovic, Siegfried Selberherr *

Institute for Microelectronics, TU Wien, Gußhausstraße 27-29/E360, 1040 Wien, Austria

ARTICLE INFO

Article history:

Received 23 August 2015

Accepted 14 September 2015

Available online 26 September 2015

Keywords:

Gas sensor

Tin oxide SnO₂

Spray pyrolysis

Power dissipation

Micromachined microheaters

Residual stress

Suspended membrane reliability

ABSTRACT

The ability to incorporate gas sensing devices into always-on wearable technology such as smart phones, tablets, and wrist watches will revolutionize the environmental health and safety industry by providing individuals with a convenient way to detect harmful chemicals in the environment. Although thin metal oxide films have shown their gas-sensing ability, several challenges must still be overcome in order to enable full CMOS integration with a reduced cost of production. A micromachined tin oxide (SnO₂) gas sensor on a suspended membrane is presented and its operation, heat flux away from the membrane, and stress generation are analyzed. The device operates based on the adsorption of oxygen at its surface when heated to temperatures between 250 °C and 550 °C, where the presence of oxygen ions results in the formation of a depletion region inside the SnO₂ layer. The thermal flux away from the heated membrane is calculated, resulting in a total power loss of 32.5 mW. In this calculation, the heat flux through the membrane as well as the air conduction and radiation are accounted for. The stress through the membrane is calculated to be around 500 MPa to 550 MPa with a maximum displacement of 6.6 μm through its middle. The intrinsic stress through the tin oxide layer is analyzed during film growth using the Volmer-Weber model, resulting in a 200 MPa stress and a 1.69 J/m² surface free energy of the deposited material. The use of spray pyrolysis, a CMOS-friendly deposition technique, in order to deposit the SnO₂ layer on the membrane resulted in a total thermo-mechanical stress of 380 MPa.

© 2015 Elsevier Ltd. All rights reserved.

1. Introduction

The presence of multiple gases in our vicinity shapes our perception of the environment. Although the human nose serves as a sensor or detector of hundreds of different odours, it fails when absolute gas concentrations or odourless gases require detection. The ability to electrically detect these gases is a topic of extensive research and has found applications in areas related to increased comfort, such as climate controls in buildings and vehicles, but also in safety. The feasibility to detect toxic and harmful gases in our environment through hand held and wearable devices is of particular significance triggering substantial research. In addition, fabrication and process controls, and laboratory analytics can be made more affordable with cheaper gas sensing equipment [1].

Currently, a variety of gas sensing principles are being implemented in industry, e.g. semiconductor, optical, thermal conductivity, quartz microbalance, catalytic, dielectric, electrochemical, and electrolyte sensors [1]. Recent discoveries in the use of metal oxides as gas sensing materials are at the forefront for enabling significant progress in moving away from bulky sensor architectures [1–10]. The miniaturization of electronic devices has proven to be essential, while the gas sensor field is still lagging behind the overall progress of CMOS and MEMS devices. Two materials have been validated to exhibit all the properties required for a good

gas sensing performance, namely zinc oxide (ZnO) [11–14] and tin oxide (SnO₂) [15–17], while others such as indium tin oxide (ITO), In₂O₃, CdO, ZnSnO₄, NiO, etc. have also been widely studied [13]. These studies attempt to drive research towards the fabrication of cheap, small, and user-friendly devices with a high sensitivity, selectivity, and stability with respect to the desired application. However, before true integration of gas sensor components inside gadgets such as smart phones and wrist watches can be achieved, several challenges must be overcome:

- Until recently, gas sensor fabrication was not compatible with that of a conventional CMOS process sequence, which is essential for its integration into hand-held electronics. Currently, the deposition of metal oxide materials is being performed using several techniques such as chemical vapor deposition [18], sputtering [19], pulsed-laser deposition [20], sol-gel process [21], rheotaxial growth and vacuum oxidation [22], and spray pyrolysis [15].
- Thin metal-oxide layers can only act as gas sensors when heated to temperatures between 250 °C and 550 °C, which means that a micro-hotplate must accompany each sensor. The integration of the hotplate and the sensor with the required analog and digital circuitry, as shown in Fig. 1, is necessary. Since metal oxides detect various gases, a sensor array is implemented in order to introduce selectivity in the sensor unit [23].

As already depicted in Fig. 1 the operation of a smart gas sensor implies the ability to detect a multitude of hazardous gases in the environment, for which multiple sensor circuits are required. The analog signals

* Corresponding author.

E-mail address: Selberherr@iue.tuwien.ac.at (S. Selberherr).

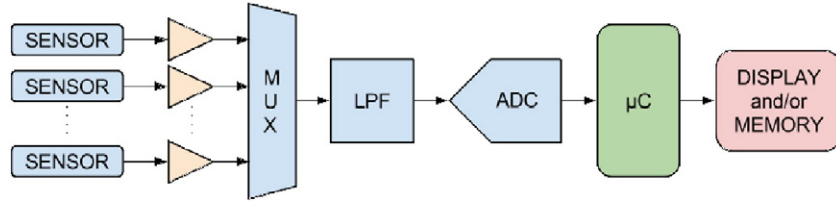


Fig. 1. Sensor unit showing a sensor array with interface electronics blocks, which include the amplifiers, multiplexer (MUX), low-pass filter (LPF), analog to digital converter (ADC), microcontroller (μC), and DISPLAY and/or MEMORY.

from these sensors are passed through an amplifier to a multiplexer. The output from the multiplexer is sent through a low-pass filter (LPF) and an analog to digital converter (ADC) before the signal can be analyzed with a microcontroller (μC) and eventually displayed or stored [7]. Although the major part of the electronics consists of analog and digital CMOS circuitry, the most complex component for integration and manufacturing is the sensor itself.

In this work several aspects of a typical tin oxide gas sensor are analyzed with the aid of simulation in order to understand the sensor performance and reliability with regard to thermal dissipation and stress build-up. First, the gas sensor analyzed in this work and the sensing mechanism itself are described. A model for a compact thin-film SnO_2 sensor is presented for the detection of ambient H_2 , which is an important component in smoke and fire detectors. Afterwards, the reliability of the suspended membrane is discussed, where the thermal dissipation of the device is analyzed and essential design components are given in order to minimize the power dissipation. The stress build-up in the membrane is also discussed, followed by an analysis of the stress build-up in the metal oxide during deposition, according to the Volmer-Weber growth mode [24].

2. Metal oxide sensor operation

At increased temperatures, oxygen is adsorbed at the metal oxide surface by trapping electrons from the bulk material [25]. The result is an overall decrease or increase in the metal oxide resistance, depending on whether the material is n-type or p-type, respectively. The band bending at the metal oxide/ambient interface is depicted in Fig. 2. The introduction of a target gas in the atmosphere causes a reaction with the oxygen, removing it from the interface and reducing the band bending effect and thereby the overall resistance [26].

The thickness of the depletion layer is in the order of the Debye length, defined as

$$\lambda_D = \sqrt{\frac{\epsilon \cdot k_B \cdot T}{q^2 \cdot n_c}} \quad (1)$$

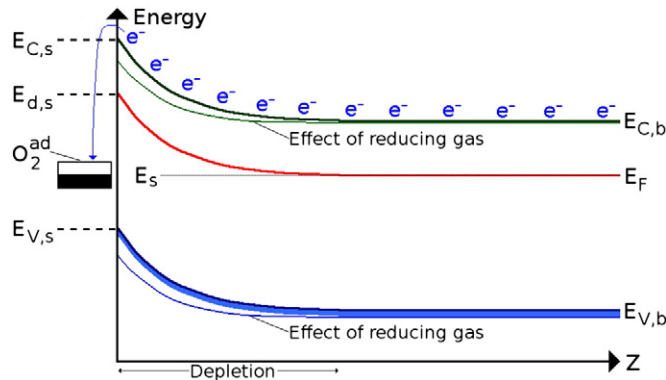


Fig. 2. Schematic representation of the band bending effect caused by oxygen adsorption and subsequent introduction of a reducing gas.

where ϵ_0 is the free space permittivity, q is the elementary charge, and n_c is the carrier charge density.

Even though plenty of effort has been directed towards understanding the gas sensing function of metal oxide materials, the exact chemistry of the sensing process is complex and not yet exhaustively understood [27]. The thin film can either be porous, where sensing occurs at the grain-level and between individual grains, or compact, where sensing occurs on the bulk material surface, as depicted in Fig. 3. A porous film is more complex to deposit when compared to a compact thin film, usually involving a sol-gel technique followed by a gelation step [27]. More recently, rheotaxial growth and vacuum oxidation was used to deposit porous films [22]. A compact metal oxide thin film can be deposited using a variety of techniques, including spray pyrolysis which has recently gained traction due to its cost-effectiveness and integration within a standard CMOS processing sequence. This study concerns itself with a compact tin oxide metal film, deposited on a micromachined suspended membrane.

2.1. SnO_2 gas sensor geometry

The geometry of the sensor studied here is depicted in Fig. 4. The membrane has an area of $200 \mu\text{m} \times 200 \mu\text{m}$ while the active sensor area is $100 \mu\text{m} \times 100 \mu\text{m}$. The beams connecting the membrane to the wafer are $100 \mu\text{m}$ long and $20 \mu\text{m}$ wide. The thicknesses of the membrane and the beams are $4 \mu\text{m}$ with a microheater sandwiched between a $2 \mu\text{m}$ SiO_2 layer at the bottom and a $2 \mu\text{m}$ Si_3N_4 layer at the top. The

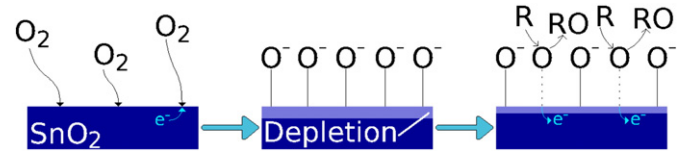


Fig. 3. Gas sensing function for a compact tin oxide film. The reaction occurs only at the top surface of the deposited tin oxide. The symbol R refers to a reducing gas.

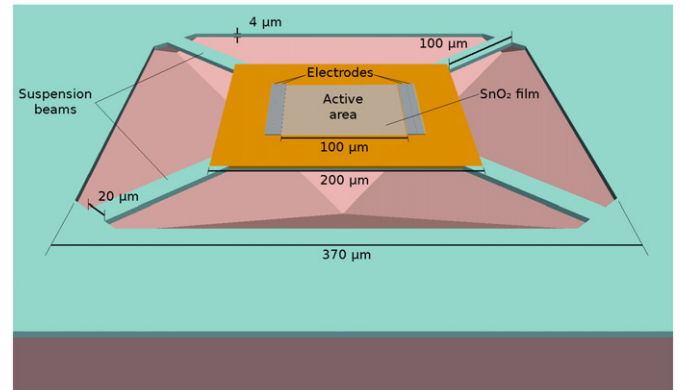


Fig. 4. Setup of the integrated gas sensor on top of a micromachined suspended membrane.

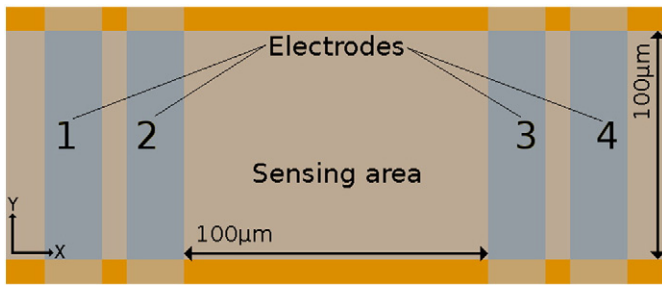


Fig. 5. Top view of the electrode locations on the substrate with the sensing area (SnO_2) deposited on top of four electrodes. The sensing area is $100 \mu\text{m} \times 100 \mu\text{m}$.

aluminum electrodes and a 50 nm thin tin oxide film are deposited on top of the Si_3N_4 layer above the microheater location.

The top view of the sensing area is shown in Fig. 5, where four electrodes are evident. Four-electrode sensing is used for increased sensitivity and added accuracy, while eliminating the lead and contact resistances [28].

2.2. SnO_2 gas sensing capability

The gas sensing capability of SnO_2 is well known and it is the most common metal oxide used for the detection of harmful gases [1,29]. This is in part due to its sensitivity to a broad range of gases, but also due to the ability of the material to be deposited on a silicon substrate using a variety of simple and inexpensive methods. Fig. 6 shows the response of a SnO_2 thin film to the presence of hydrogen [16] and carbon monoxide [30] in the environment.

The SnO_2 sensor response to the presence of CO shown in the top plot in Fig. 6 has been measured at 400°C for a film which was deposited using a spray and includes impurities in the form of Pt nanoparticles [31]. The effect of the Pt impurity and higher operating temperature is noted by an increase in the sensing performance by almost ten times. The symbols in Fig. 6 represent measured data while the solid lines correspond to power regression lines of best fit.

The measured resistances from Fig. 6 are a combination of the contact resistance in series with a parallel combination of the bulk and depletion region resistances, depicted in Fig. 7 [32]. Due to the four-terminal sensing used in this study the contact resistances are

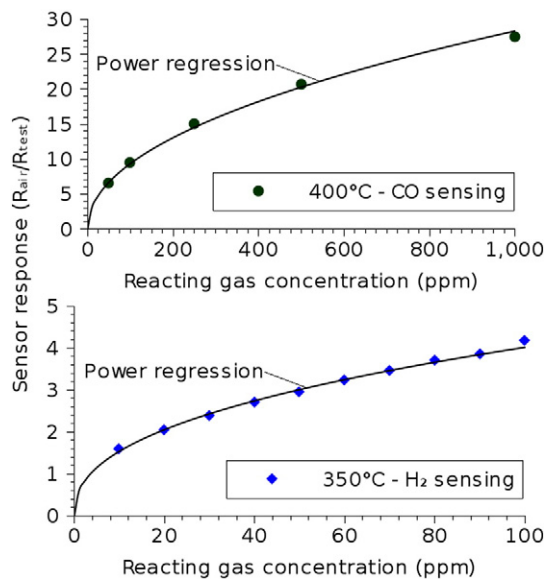


Fig. 6. SnO_2 thin film sensor response dependence on the concentrations of H_2 and CO reacting gases. The temperatures used during measurement correspond to the optimal temperature of operation for the detection of the particular gas.

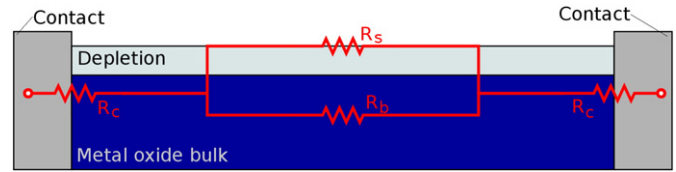


Fig. 7. Resistances acting during the operation of a metal oxide gas sensor.

neglected, meaning that the resistance is a parallel combination of the bulk resistance R_b – the gas-unaffected region with an unchanged resistivity – and the depletion region resistance R_s – equivalent to the geometric surface which is affected by the gas reaction [1].

Because the bulk resistance is much smaller than the resistance of the depletion region, the overall sensor resistance is mainly controlled by the bulk resistance and therefore, by the thickness of the bulk region – or inversely by the thickness of the depletion region. At room temperature, the resistance of the sensor presented in Section 2.1 was measured to be $10.7 \text{ k}\Omega$, suggesting a tin oxide conductivity of 1.6 kS/m (or a resistivity of $0.625 \text{ m}\Omega\cdot\text{m}$). This value is in the range of values suggested by several experimental groups [33,34]. When the material is heated to 350°C in an oxygen-rich environment, the resistance increased to $30 \text{ k}\Omega$ [16]. Assuming the resistivity of the bulk remains $0.625 \text{ m}\Omega\cdot\text{m}$, the thickness of the material must be 13 nm in order for the resistance to reach $30 \text{ k}\Omega$. Therefore, the increased temperature leads to the adsorption of oxygen at the surface and the generation of a 37 nm -thick depletion region. Following Eq. (1) the carrier charge density is found to be $2.3 \times 10^{22} \text{ m}^{-3}$. A plot of how the resistance of the sensor layer changes with increasing depletion layer thickness is given in Fig. 8. Introducing a reducing agent, such as H_2 or CO, will lead to the reduction of the depletion region and thereby the reduction of the sensor resistance.

3. Thermal reliability of the MEMS membrane

Micromachining metal oxide gas sensors has become very promising in overcoming the difficulties of screen printing ceramic sensors. Screen-printed ceramic devices require a typical power consumption in the range of 200 mW to 1 W [1], which is too high for battery-operated devices. Micromachined sensors typically require a power consumption in the range between 30 mW and 150 mW [1].

3.1. Thermal transport

The loss of heat from the device is a major concern in the design of micromachined sensors. There are several heat “escape routes” which can increase the power requirements for a given device. The main

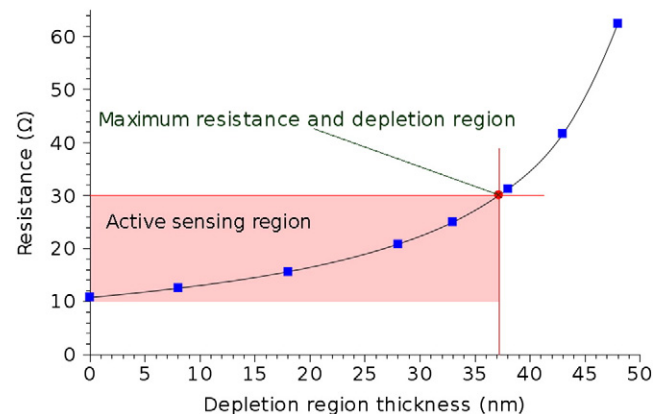


Fig. 8. The changing resistance of a thin $100 \mu\text{m} \times 100 \mu\text{m}$ SnO_2 sheet as a circumstance of an increasing depletion region.

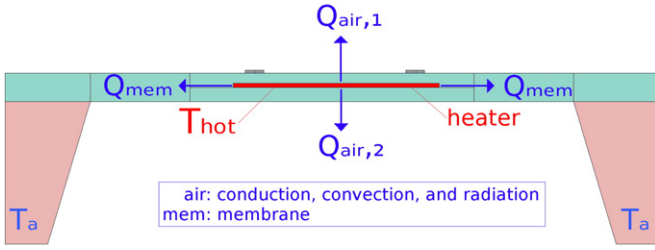


Fig. 9. Schematic representation of the heat flux through a micromachined gas sensor. Q_{air} is the combined conduction, convection, and radiation heat flux through the air; Q_{mem} is the heat conduction through the membrane and connecting beams; T_{hot} is the microheater temperature; T_a is the ambient temperature.

heat flux components are shown in Fig. 9, where the heat loss through the membrane and the connecting beams Q_{mem} and the heat loss in the air Q_{air} are the main components. The flux through the air is a combination of the heat lost to conduction, convection, and radiation. In this section, the heat fluxes are calculated and the total required power is calculated for the sample device with the geometry given in Section 2.1.

The equations used for the calculation of the heat dissipation through the membrane summarized here are explained in further detail in the work of Simon et al. [1]. The heat conduction through the membrane is given by

$$Q_{mem} = \frac{4 \cdot \lambda_m \cdot A_{beam} (T_{hot} - T_a)}{l}, \quad (2)$$

where λ_m is the thermal conductivity of the membrane, A_{beam} is the cross-sectional area of the connecting beam, and l is the membrane and beam thickness. To estimate the heat losses in the air, fluid motion is neglected, as is assumed by many authors [1], which means that the convection component can be neglected. The conduction component for the top and bottom surfaces must be treated separately. The loss due to air conduction through the top of the membrane is given by

$$Q_{cond,top} = \frac{4 \cdot \pi \cdot \lambda_{air} (T_{hot} - T_a)}{1/r_i - 1/r_a}, \quad (3)$$

where λ_{air} is the thermal conductivity of air and r_i and r_a refer to the effective radii of the heated area and the full membrane, respectively, when the rectangular areas are converted to round ones. This conversion effectively reduces the two-dimensional problem to a one-

Table 1

Parameter values used to calculate the heat flux of the sample micromachined sensor structure required for Eqs. (2), (3), (4), and (5).

Parameter	Value	Units	Description
λ_m	10	W/Km	Membrane thermal conductivity
λ_a	0.026–0.044	W/Km	Air thermal conductivity
l	100	μm	Membrane thickness
T_{hot}	400	$^{\circ}\text{C}$	Heater temperature
T_a	20	$^{\circ}\text{C}$	Ambient temperature
r_i	56.4	μm	Equivalent heated area radius
r_a	112.8	μm	Equivalent membrane radius
h	100	μm	Pit depth
σ	5.67×10^{-8}	$\text{W/m}^2\text{K}^4$	Stefan-Boltzmann constant
ε	0.7	-	Emissivity

Table 2

Heat fluxes for the components given in Fig. 9.

Heat flux	Value (mW)
Q_{mem}	12.216
$Q_{cond,top}$	18.859
$Q_{cond,bottom}$	1.330
$Q_{radiation}$	0.157
Q_{TOTAL}	32.506

dimensional one. The conduction through the bottom of the membrane is given by

$$Q_{cond,bottom} = \frac{\lambda_{air} \cdot A_{hot} (T_{hot} - T_a)}{h}, \quad (4)$$

where A_{hot} is the area of the heated section of the membrane and h is the distance between the bottom membrane and the die, or the depth of the air pit. The radiation component of the heat flux is expressed by

$$Q_{radiation} = G_{radiation} \cdot \sigma \cdot \varepsilon (T_{hot}^4 - T_a^4), \quad (5)$$

where $G_{radiation}$ is a geometry factor which can be set to $2 \cdot A_{hot}$ [1], σ is the Stefan-Boltzmann constant, and ε is the emissivity. The heat flux emission from a suspended membrane above a silicon die is depicted in Fig. 10. The material and geometric properties of the simulated device are given in Table 1 along with the resulting heat flux components, corresponding to Eqs. (2), (3), (4), and (5) in Table 2. The total power dissipation for

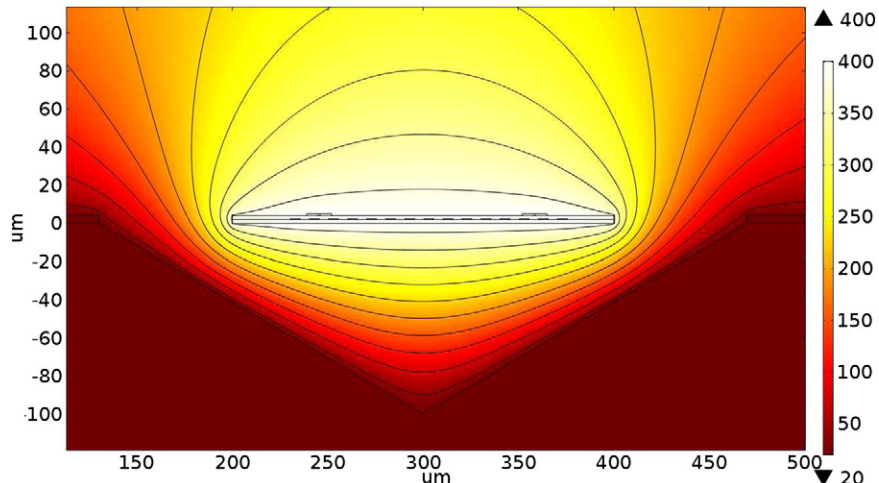


Fig. 10. Heat flux emission lines from a central suspended membrane.

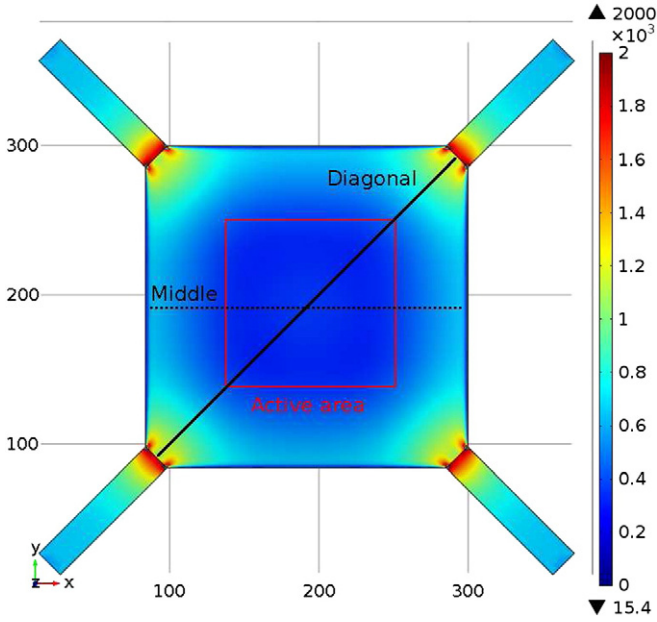


Fig. 11. Stress distribution through the sensor membrane when 1 GPa and -320 MPa residual stresses are observed in the Si_3N_4 and SiO_2 layers, respectively.

the presented design is approximately 32.5 mW; however, this value can be reduced using more complex microheater structures [35].

3.2. Membrane stress

The stress in the semiconductor membrane is a combination of the residual stresses in the layers which make up the complete membrane. The control of the residual stress in single layers and especially multilayer systems such as the micromachined membrane presented here is crucial for its stability [36]. Typical values for the residual stress in Si_3N_4 (1 GPa [37]) and SiO_2 (-320 MPa [38]) films are applied and the stress distribution in the full membrane with beams is simulated in a finite element environment.

The resulting stress through the membrane is plotted in Fig. 11 and the one-dimensional cut lines of the stress through the middle of the membrane and diagonally through the membrane are shown in Fig. 12. The resulting average stress is found to be 435 MPa with an

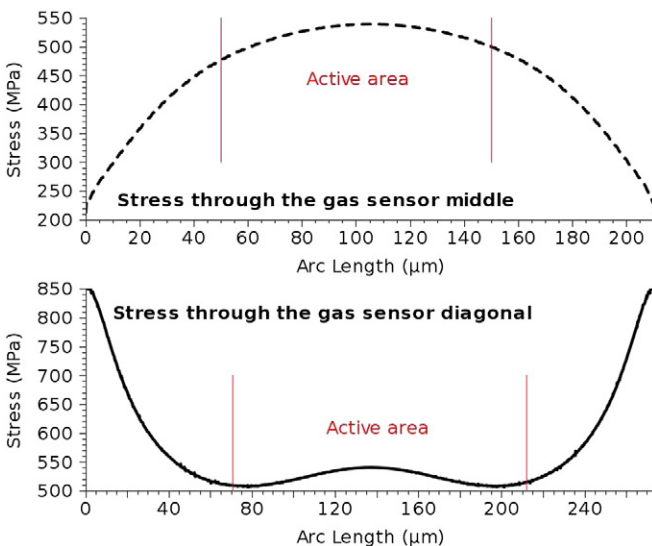


Fig. 12. Stress distribution through the middle and diagonally through the sensor structure from Fig. 11.

average displacement of 4.1 μm . The maximum displacement was noted through the middle of the membrane to be 6.6 μm . The stress through the active region of the membrane varies between 500 MPa and 550 MPa with the stress increasing towards the beams.

4. Stress in thin SnO_2 layers

During deposition of the metal oxide thin films, a stress builds up, which can have negative effects on the device reliability. The post-processing stress in a thin film is a result of two stress components: the intrinsic stress, which arises during the film growth, and the thermo-mechanical stress, which is a result of the difference in the deposition temperature and the subsequent cooling to room temperature. The thermo-mechanical stress is a concern, when high temperatures are used for the metal oxide deposition due to the difference in the coefficients of thermal expansion (CTE) between the depositing material and the silicon substrate. The growth mode of thin films depends on the surface free energy of the deposit, the substrate, and the interface between the two materials. The growth process is characterized by the Volmer-Weber growth mode [39,40], where small islands of the depositing film form on the surface, which through expansion impinge on each other, eventually forming a coalesced thin film. Due to the surface interaction between the materials and the impingement of the depositing islands, a stress forms in the thin film [24].

4.1. Intrinsic stress in thin metal films

During the deposition of metals and metal oxides on oxidized silicon surfaces, the film deposits in the form of islands which coalesce and then grow to form larger grains, a process known as Volmer-Weber growth mode [24,40]. The intrinsic stress generated during thin film growth develops during deposition and can go through stages of compressive and tensile stresses depending on the film properties. Fig. 13 summarizes the main steps involved in the film growth, as characterized in [24].

The initial stage is the island nucleation or the formation of small islands on the surface. As the islands grow, they impinge on each other, which generates tensile stress in the islands. When all the islands on the surface are connected, a film is said to have coalesced. The next stage of growth is the film thickening which can be either columnar or polycrystalline. The columnar thickening mode shown in Fig. 13(d) refers to the growth of films which have a high adatom mobility or low melting temperatures, such as silver (Ag), copper (Cu), and aluminum (Al). The polycrystalline growth shown in Fig. 13(e) refers to the growth of films which have a low adatom mobility or high melting temperatures, such as tungsten (W), chromium (Cr), and tantalum (Ta). Before film coalescence, there are two main stress components to consider, namely the compressive stress which is generated due to the island nucleation and the tensile stress generated in the thin film due to island impingement. The evolution of the stress during growth of the two types of materials is shown in Fig. 14. The generation of compressive stresses during nucleation and thickening as well as the generation of a tensile stress during coalescence is depicted. The intrinsic stress of materials with low adatom mobility does not vary after coalescence and remains constant during thickening. However, materials with high adatom mobility experience a reduced stress, or increased compressive stress, during post-coalescence film growth.

During the formation and subsequent radial expansion of an island in the course of film growth a compressive stress builds up due to an excess in surface energy. The model which governs the build-up of compressive stress in relation to the growth of an island is given in [24] as

$$\sigma_{\text{compressive}} = -\frac{2f}{r} \cdot \frac{\sin\theta}{(1-\cos\theta)(2+\cos\theta)}, \quad (6)$$

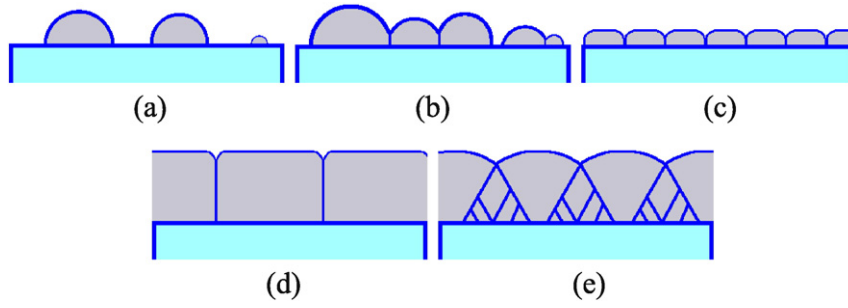


Fig. 13. Steps during film formation in the Volmer-Weber growth mode. (a) 1-nucleation (b) 2-impingement (c) 3-coalescence (d) 4a-thickening (e) 4b-thickening.

where $f = \gamma_{gb} - 2\gamma_s$ is the surface stress (γ_{gb} is the grain boundary energy and γ_s is the surface energy), r is the island radius, and θ is the contact angle between the island surface and the substrate, depicted in Fig. 15. Upon island impingement a grain boundary is formed between two islands, which results in a part of the free surface of each island being eliminated and in a significant energy reduction. This process of zipping at the grain boundary to a specific height generates tensile stress in the grains. Fig. 15 shows the process of two islands impinging on each other and the formation of a grain boundary. When two islands approach each other and each attempts to increase its radius, a grain boundary forms. The generated tensile stress depends on the resulting geometry of that process, given in [24] as

$$\sigma_{tensile} = \frac{1}{2} \cdot \frac{E}{1-r^2} \left(\frac{y_0}{r} \right)^{1.3892}, \quad (7)$$

where E is the Young's modulus, and r and y_0 are geometric parameters given in Fig. 15. When two islands come together (Step 1 in Fig. 15) and they attempt to grow, each island will be hindered by the presence of the adjacent island. Therefore, instead of freely expanding its circumference, a vertical boundary will form between them, with a height z_0 (Step 2 in Fig. 15).

4.2. Intrinsic stress in the SnO_2 sensing layer

In this section the sputter and spray pyrolysis deposition of thin tin oxide films is discussed.

4.2.1. Sputter deposition

During the sputter deposition at approximately 70° with a low oxygen content in the sputtering gas, the stress is found to be 200 MPa [19]. The stress development during film growth is analyzed using Eqs. (6) and (7). In Fig. 16 the stress evolution during film growth can be seen. Because the stress is difficult to estimate in the early stages of film growth, below 5 nm, the stress-thickness ($\sigma \cdot h$) parameter is

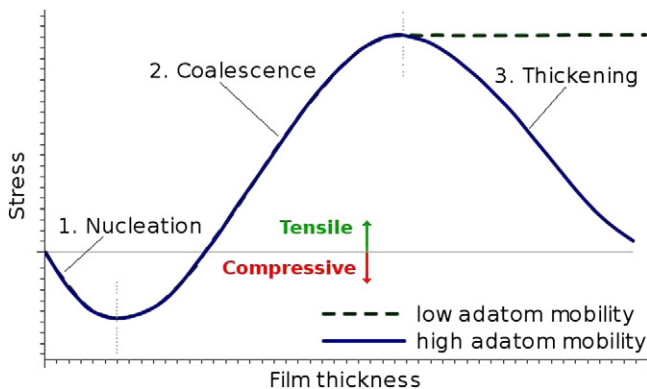


Fig. 14. Stress evolution during the growth of metal and metal oxide films.

used instead. The compressive and tensile stress components are tracked from the early stages of film growth with the parameters given in Table 3. Using the intrinsic stress simulation, a value of 1.69 J/m^2 for the surface free energy of the tin oxide film is calculated.

The thermal stress is then calculated using finite element methods and applying a cooling to the layer from 70° to room temperature. The thereby added stress is 50 MPa, resulting in a total residual stress of 250 MPa in the tin oxide layer.

4.2.2. Spray pyrolysis deposition

During spray pyrolysis deposition the wafer is heated to 400°C , while a gas pressure nozzle is used to spray a $\text{SnCl}_4 + \text{H}_2\text{O}$ solution towards it for a 30 s burst. Due to the temperature used, the intrinsic stress is less of a concern and the thermal stress should play a larger role. A simulation is performed by cooling the device from the deposition temperature to room temperature with a resulting stress of 380 MPa. Although the stress in the sputtered film is slightly lower, the spray pyrolysis method is much more cost effective. Also, the sputter deposition used is in a low oxygen environment, resulting in a slower deposition process, while regular sputter deposition usually results in films with an intrinsic stress in the 1 GPa range [19].

5. Conclusion

The integration of gas sensors in hand-held devices requires fabrication techniques to be compatible with the CMOS sequence, the power dissipation to be suitable for battery-powered technologies, and a minimal stress build up due to reliability concerns. A performance and reliability analysis of a micromachined gas sensor with a suspended membrane and tin oxide as the sensing layer was performed using simulations. A sample device was presented with a membrane area of $200 \mu\text{m} \times 200 \mu\text{m}$, an active sensor area of $100 \mu\text{m} \times 100 \mu\text{m}$, and a membrane thickness of $4 \mu\text{m}$, which is composed of equally thick silicon nitride and silicon dioxide.

Based on several experimental studies and measured results from the operation of a tin oxide sensor, simulations were performed to gain further understanding in the sensing material itself. It was noted

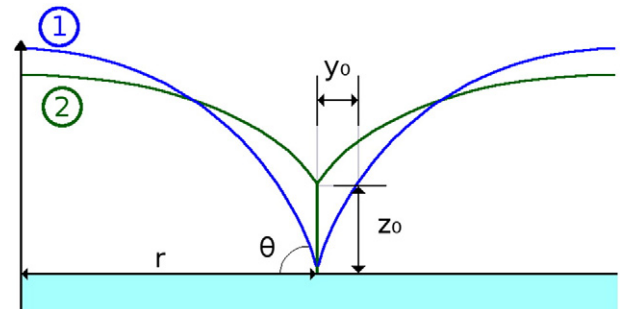


Fig. 15. From Position 1 to Position 2, two islands impinge, resulting in a grain boundary with height z_0 .

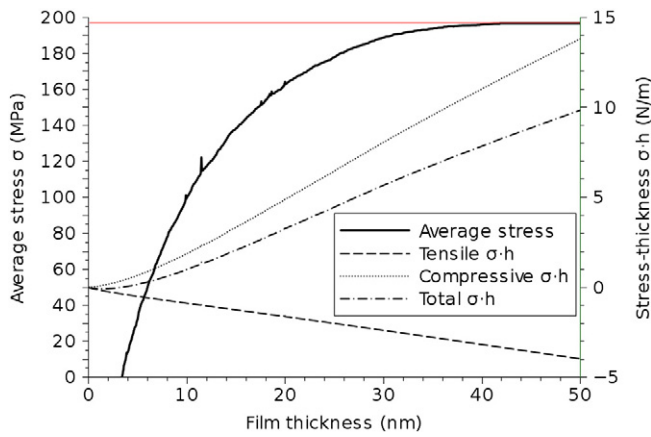


Fig. 16. Intrinsic stress generation during sputter deposition of tin oxide thin films at 70°. The stress-thickness ($\sigma \cdot h$) product is used in order to accurately observe the stress before film coalescence.

that a tin oxide layer deposited using spray pyrolysis has a resistivity of 0.625 m $\Omega \cdot \text{m}$ and a resistance of 10.7 k Ω . However, during operation, a maximum resistance of 30 k Ω is noted, suggesting the formation of a 37 nm depletion region, which corresponds to a carrier charge density of $2.3 \times 10^{22} \text{ m}^{-3}$. The introduction of reactant gases in the environment reduces the effective carrier charge density on the tin oxide surface and thereby also the overall tin oxide resistance.

An analysis of the thermal reliability of the suspended membrane resulted in a total power dissipation of 32.5 mW for the sample device. This amount is a combination of the heat conduction, convection, and radiation into the air above and below the membrane, as well as the heat dissipation through the beams which attach the membrane to the silicon wafer. This heat dissipation level is in a low range for micromachined sensors, while it is significantly lower than screen-printed ceramics which require a power consumption in the range of 200 mW to 1 W. The average stress through the suspended membrane was found to be 435 MPa with a maximum displacement of 6.6 μm in the middle of the membrane.

The stress generation during the growth of tin oxide has also been examined for sputter and spray pyrolysis deposition techniques. The post-processing stress is a combination of the intrinsic stress, which develops during the Volmer-Weber film growth, and the thermo-mechanical stress, which develops as a result of material cooling to room temperature from a thermal deposition step. A post-processing stress for sputtered films was found to be 250 MPa, leading to a value of 1.69 J/m² for the surface free energy of the tin oxide film. Alternatively, the spray pyrolysis deposition resulted in a post-processing stress of 380 MPa, mainly due to the thermo-mechanical stress after cooling the device to room temperature from its 400 °C processing temperature.

Table 3

Material properties of tin oxide, required for the simulation of the intrinsic stress evolution during film growth.

Characteristic	Value for a SnO ₂ film	Ref.
Young's modulus E	253 GPa	[41]
Poisson's ratio ν	0.293	[41]
Coefficient of thermal expansion (CTE) α	$4.0 \times 10^{-6} \text{ K}^{-1}$	[29]
Density ρ	6.99 g/cm ³	[29]
Average grain size D	15 nm	[42]
Melting point	1900 °C	[29]
Intrinsic stress σ_i	200 MPa	[19]
Surface free energy f	1.69 J/m ²	
Contact angle θ	80°	
Thermo-mechanical stress σ_{th}	50 MPa	

References

- [1] I. Simon, N. Bârsan, M. Bauer, U. Weimar, Micromachined metal oxide gas sensors: opportunities to improve sensor performance, *Sens. Actuators B Chem.* 73 (1) (2001) 1–26.
- [2] M. Frietsch, F. Zudock, J. Goschnick, M. Bruns, CuO catalytic membrane as selectivity trimmer for metal oxide gas sensors, *Sens. Actuators B Chem.* 65 (1) (2000) 379–381.
- [3] N. Barsan, U. Weimar, Conduction model of metal oxide gas sensors, *J. Electroceram.* 7 (3) (2001) 143–167.
- [4] G. Korotcenkov, V. Brinzari, J. Schwank, M. DiBattista, A. Vasiliev, Peculiarities of SnO₂ thin film deposition by spray pyrolysis for gas sensor application, *Sens. Actuators B Chem.* 77 (1) (2001) 244–252.
- [5] E. Comini, Metal oxide nano-crystals for gas sensing, *Anal. Chim. Acta* 568 (1) (2006) 28–40.
- [6] N. Barsan, D. Koziej, U. Weimar, Metal oxide-based gas sensor research: how to? *Sens. Actuators B Chem.* 121 (1) (2007) 18–35.
- [7] J.W. Gardner, P.K. Guha, F. Udrea, J.A. Covington, CMOS interfacing for integrated gas sensors: a review, *IEEE Sens. J.* 10 (12) (2010) 1833–1848.
- [8] C. Wang, L. Yin, L. Zhang, D. Xiang, R. Gao, Metal oxide gas sensors: sensitivity and influencing factors, *Sensors* 10 (3) (2010) 2088–2106.
- [9] C. Pijolat, Metal oxide gas sensors, *Chem. Sens. Biosens.* (2012) 93–125.
- [10] G. Korotcenkov, *Handbook of Gas Sensor Materials*. 1em plus 0.5em minus 0.4em, Springer, 2014 47–71.
- [11] M. Ortel, Y.S. Trostyanskaya, V. Wagner, Spray pyrolysis of ZnO-TFTs utilizing a perfume atomizer, *Solid State Electron.* 86 (2013) 22–26.
- [12] S. Shinde, G. Patil, D. Kajale, V. Gaikwad, G. Jain, Synthesis of ZnO nanorods by spray pyrolysis for H₂S gas sensor, *J. Alloys Compd.* 528 (2012) 109–114.
- [13] A. Bouaoud, A. Rmili, F. Ouachtari, A. Louardi, T. Chtouki, B. Elidrissi, H. Erguig, Transparent conducting properties of Ni doped zinc oxide thin films prepared by a facile spray pyrolysis technique using perfume atomizer, *Mater. Chem. Phys.* 137 (3) (2013) 843–847.
- [14] M. Prasad, V. Sahula, V. Khanna, Design and fabrication of Si-diaphragm, ZnO piezoelectric film-based MEMS acoustic sensor using SOI wafers, *IEEE Trans. Semicond. Manuf.* 26 (2) (2013) 233–241.
- [15] G. Patil, D. Kajale, V. Gaikwad, G. Jain, Spray pyrolysis deposition of nanostructured tin oxide thin films, *ISRN Nanotechnol.* 2012 (2012).
- [16] G. Mutinati, E. Brunet, S. Steinhauer, A. Köck, J. Teva, J. Kraft, J. Siebert, F. Schrank, E. Bertagnolli, CMOS-integrable ultrathin SnO₂ layer for smart gas sensor devices, *Prod. Eng.* 47 (2012) 490–493.
- [17] E. Brunet, T. Maier, G. Mutinati, S. Steinhauer, A. Köck, C. Gspan, W. Grogger, Comparison of the gas sensing performance of SnO₂ thin film and SnO₂ nanowire sensors, *Sens. Actuators B Chem.* 165 (1) (2012) 110–118.
- [18] I. Volintiru, A. de Graaf, J. Van Deelen, P. Poort, The influence of methanol addition during the film growth of SnO₂ by atmospheric pressure chemical vapor deposition, *Thin Solid Films* 519 (19) (2011) 6258–6263.
- [19] J. Boltz, D. Koehl, M. Wuttig, Low temperature sputter deposition of SnO₂/Sb films for transparent conducting oxide applications, *Surf. Coat. Technol.* 205 (7) (2010) 2455–2460.
- [20] S. Sinha, R. Bhattacharya, S. Ray, I. Manna, Influence of deposition temperature on structure and morphology of nanostructured SnO₂ films synthesized by pulsed laser deposition, *Mater. Lett.* 65 (2) (2011) 146–149.
- [21] D.M. Carvalho, J.L. Maciel Jr., L.P. Ravar, R.E. Garcia, V.G. Ferreira, L.V. Scalvi, Numerical simulation of the liquid phase in SnO₂ thin film deposition by sol-gel-dip-coating, *J. Sol-Gel Sci. Technol.* 55 (3) (2010) 385–393.
- [22] M. Kwoka, M. Krzywiecki, Rheotaxial growth and vacuum oxidation – novel technique of tin oxide deposition – in situ monitoring of oxidation process, *Mater. Lett.* 154 (2015) 1–4.
- [23] U. Hofer, H. Böttner, A. Felske, G. Kühner, K. Steiner, G. Sulz, Thin-film SnO₂ sensor arrays controlled by variation of contact potential – a suitable tool for chemometric gas mixture analysis in the TLV range, *Sens. Actuators B Chem.* 44 (1) (1997) 429–433.
- [24] S.C. Seel, Stress and Structure Evolution During Volmer-Weber Growth of Thin Films, Ph.D. dissertation, Massachusetts Institute of Technology, 2002.
- [25] L. Filipovic, S. Selberherr, Performance and stress analysis of metal oxide films for CMOS-integrated gas sensors, *Sensors* 15 (4) (2015) 7206–7227.
- [26] N. Barsan, U. Weimar, Fundamentals of metal oxide gas sensors, *Tagungsband* (2012) 618–621.
- [27] M. Tiemann, Porous metal oxides as gas sensors, *Chem. A Eur. J.* 13 (30) (2007) 8376–8388.
- [28] H. Liu, J. Kameoka, D.A. Czaplewski, H. Craighead, Polymeric nanowire chemical sensor, *Nano Lett.* 4 (4) (2004) 671–675.
- [29] M. Batzill, U. Diebold, The surface and materials science of tin oxide, *Prog. Surf. Sci.* 79 (2) (2005) 47–154.
- [30] M. Di Giulio, G. Micocci, R. Rella, P. Siciliano, A. Tepore, Properties of reactively sputtered tin oxide films as CO gas sensors, *Sens. Actuators B Chem.* 23 (2) (1995) 193–195.
- [31] L. Mädler, T. Sahn, A. Gurlo, J.-D. Grunwaldt, N. Barsan, U. Weimar, S. Pratsinis, Sensing low concentrations of CO using flame-spray-made Pt/SnO₂ nanoparticles, *J. Nanoparticle Res.* 8 (6) (2006) 783–796.
- [32] G. Chabanis, I.P. Parkin, D.E. Williams, A simple equivalent circuit model to represent microstructure effects on the response of semiconducting oxide-based gas sensors, *Meas. Sci. Technol.* 14 (1) (2003) 76.
- [33] K. Shamala, L. Murthy, K.N. Rao, Studies on tin oxide films prepared by electron beam evaporation and spray pyrolysis methods, *Bull. Mater. Sci.* 27 (3) (2004) 295–301.

- [34] J. Joseph, V. Mathew, J. Mathew, K. Abraham, Studies on physical properties and carrier conversion of SnO₂:Nd thin films, *Turk. J. Phys.* 33 (2009) 37–47.
- [35] M. Siegele, C. Gamauf, A. Nemecek, G.C. Mutinati, S. Steinhauer, A. Kock, J. Kraft, J. Siezert, F. Schrank, Optimized integrated micro-hotplates in CMOS technology, *Proceedings of the 11th IEEE International New Circuits and Systems Conference* 2013, pp. 1–4.
- [36] H.M. Low, M.S. Tse, M.M. Chiu, Thermal induced stress on the membrane in integrated gas sensor with micro-heater, *Proceedings of the IEEE Electron Devices Meeting* 1998, pp. 140–143.
- [37] E. Irene, Residual stress in silicon nitride films, *J. Electron. Mater.* 5 (3) (1976) 287–298.
- [38] H. Leplan, J. Robic, Y. Pauleau, Kinetics of residual stress evolution in evaporated silicon dioxide films exposed to room air, *J. Appl. Phys.* 79 (9) (1996) 6926–6931.
- [39] M. Pletea, W. Brückner, H. Wendrock, R. Kaltöfen, Stress evolution during and after sputter deposition of Cu thin films onto Si (100) substrates under various sputtering pressures, *J. Appl. Phys.* 97 (5) (2005) 054908.
- [40] M. Pletea, R. Koch, H. Wendrock, R. Kaltöfen, O. Schmidt, In situ stress evolution during and after sputter deposition of Al thin films, *J. Phys. Condens. Matter* 21 (22) (2009) 225008.
- [41] G. Gladysz, K. Chawla, Coefficients of thermal expansion of some laminated ceramic composites, *Compos. A Appl. Sci. Manuf.* 32 (2) (2001) 173–178.
- [42] D.D. Vuong, G. Sakai, K. Shimano, N. Yamazoe, Preparation of grain size-controlled tin oxide sols by hydrothermal treatment for thin film sensor application, *Sens. Actuators B Chem.* 103 (1) (2004) 386–391.